ADVANCED FUNCTIONAL MATERIALS
www.afm-journal.de

High-Pressure Synthesis of Ultra-Incompressible, Hard and Superconducting Tungsten Nitrides

Akun Liang, Israel Osmond, Georg Krach, Lan-Ting Shi, Lukas Brüning, Umbertoluca Ranieri, James Spender, Ferenc Tasnadi, Bernhard Massani, Callum R. Stevens, Ryan Stewart McWilliams, Eleanor Lawrence Bright, Nico Giordano, Samuel Gallego-Parra, Yuqing Yin, Andrey Aslandukov, Fariia Iasmin Akbar, Eugene Gregoryanz, Andrew Huxley, Miriam Peña-Alvarez, Jian-Guo Si, Wolfgang Schnick, Maxim Bykov, Florian Trybel, and Dominique Laniel**

Transition metal nitrides, particularly those of 5*d* metals, are known for their outstanding properties, often relevant for industrial applications. Among these metal elements, tungsten is especially attractive given its low cost. In this high-pressure investigation of the W–N system, two novel ultra-incompressible tungsten nitride superconductors, namely W_2N_3 and W_3N_5, are successfully synthesized at 35 and 56 GPa, respectively, through a direct reaction between N_2 and W in laser-heated diamond anvil cells. Their crystal structure is determined using synchrotron single-crystal X-ray diffraction. While the W_2N_3 solid's sole constituting nitrogen species are N^{3-} units, W_3N_5 features both discrete N^{3-} as well as N_2^{4-} pernitride anions. The bulk modulus of W_2N_3 and W_3N_5 is experimentally determined to be 380(3) and 406(7) GPa, and their ultra-incompressible behavior is rationalized by their constituting WN_7 polyhedra and their linkages. Importantly, both W_2N_3 and W_3N_5 are recoverable to ambient conditions and stable in air. Density functional theory calculations reveal W_2N_3 and W_3N_5 to have a Vickers hardness of 30 and 34 GPa, and superconducting transition temperatures at ambient pressure (50 GPa) of 11.6 K (9.8 K) and 9.4 K (7.2 K), respectively. Additionally, transport measurements performed at 50 GPa on W_2N_3 corroborate with the calculations.

1. Introduction

Recently, the high-pressure synthesis of transition metal nitrides has drawn significant attention and research efforts due to their excellent mechanical and electronic properties, such as high bulk modulus,[1] high hardness,[2] high electronic conductivity, and high superconducting transition temperature (T_c).[3] In particular, some of the newly synthesized metal nitrides can be stabilized and recovered to ambient conditions, making them potential candidates for industrial applications.[2a,4]

The synthesis strategy for these hard and incompressible metal nitrides revolves around two key aspects. First, it involves utilizing 5*d* transition metals—that is, elements with a high electronic density—as starting materials. As illustrated in **Figure 1a**, these elements feature high incompressibility, with tungsten,[5] rhenium,[6] osmium,[7] and iridium[1] exhibiting a bulk modulus equal to or

A. Liang, I. Osmond, U. Ranieri, J. Spender, B. Massani, C. R. Stevens, R. S. McWilliams, E. Gregoryanz, A. Huxley, M. Peña-Alvarez, D. Laniel
Centre for Science at Extreme Conditions and School of Physics and Astronomy
University of Edinburgh
Edinburgh EH8 9YL, UK
E-mail: aliang@ed.ac.uk; dominique.laniel@ed.ac.uk

The ORCID identification number(s) for the author(s) of this article can be found under https://doi.org/10.1002/adfm.202313819

DOI: 10.1002/adfm.202313819

G. Krach, W. Schnick
Department of Chemistry
University of Munich (LMU)
81377 Munich, Germany

L.-T. Shi, J.-G. Si
Spallation Neutron Source Science Center
Dongguan 523000, P. R. China

L. Brüning, M. Bykov
Institute for Inorganic Chemistry
University of Cologne
50923 Cologne, Germany

F. Tasnadi, F. Trybel
Department of Physics, Chemistry and Biology (IFM)
Linköping University
Linköping 58183, Sweden

exceeding 300 GPa. Osmium, in particular, has been reported as the most incompressible elemental metal,[8] with literature values ranging from 397 to 462 GPa for its bulk modulus.[9] Second, the addition of nitrogen enables the formation of short covalent bonds between nitrogen and the transition metal, which not only significantly enhances the bulk modulus (as shown in Figure 1a) but also improves the material's shear modulus due to the directional nature of these bonds. Given that a material's hardness is dominantly controlled by both the bulk modulus and the shear modulus, 5*d* transition metal nitrides generally exhibit superior hardness when compared to their parent metals, as summarized in Figure 1b. Another driving force behind the synthesis of transition metal nitrides is that they typically retain their metallic nature and exhibit relatively higher values of T_c compared to their parent transition metals at ambient conditions (as shown in Table S1, Figure S1, Supporting Information). For instance, HfN has a T_c of 8.8 K at ambient conditions,[10] representing a significant increase in T_c when compared to Hf (0.17 to 0.35 K).[11] The higher T_c observed in binary transition metal nitrides can be attributed to the strengthening of electron-longitudinal-acoustic phonon coupling at a short wavelength.[12] The emergence of the superconducting state in transition metal nitrides is closely linked to the presence of anomalies in the phonon dispersion curve.[13] Materials exhibiting both super hardness and good electronic conductivity are of particular interest for a broad range of applications, such as coatings, electronic connectors, and other components working in extreme environments.

An additional criterion for transition metal nitrides regarding industrial relevance is their extraction cost. In that regard, tungsten outshines other 5*d* transition metals, being significantly cheaper—and, in particular, ≈50 times cheaper than rhenium.[16] Therefore, it does not come as a surprise that many studies have been focused on tungsten nitrides (Figure 1). Most of these nitrides have been synthesized using a large-volume press with a synthesis pressure lower than 10 GPa, such as WC-type WN,[14h] cubic-W_3N_4,[14h] $W_{2.25}N_3$,[14e] r-W_2N_3,[14h] h-W_2N_3,[14h] *c*F8-$W_{0.92}N_{0.61}$, *c*P6-$WN_{0.94}$,[14a] and MoC-type $WN_{0.6}$.[14d] Their bulk modulus varies from 226(12) GPa for r-W_2N_3[14h] to 383(5) GPa for WC-type WN.[14d] With the exception of r-W_2N_3,[14h] all tungsten nitrides have a higher or equal bulk modulus than pure tungsten. Similarly, WN, *c*P6-$WN_{0.94}$, and *c*F8-$W_{0.92}N_{0.61}$ all exhibit a hardness higher than W, having experimentally measured values of 13.8, 18, and 18 GPa, respectively.[14a,17] It can be noted that tungsten atoms in all of the aforementioned tungsten nitrides are sixfold coordinated by nitrogen atoms, forming WN_6 octahedra. Other tungsten nitrides were discovered at significantly higher pressures (i.e., >70 GPa) in laser-heated diamond anvil cell (DAC), that is, U_7Te_{12}-type W_7N_{12} (70 GPa),[4] $WN_8{\cdot}N_2$ (105 GPa)[18] and WN_6 (126–165 GPa).[14b] While W_7N_{12} and $WN_8{\cdot}N_2$ are comprised of WN_7 and WN_8 polyhedra, respectively, WN_6 contains armchair-like hexazine N_6 rings featuring N—N single bonds. Moreover, the coordination change of tungsten, from sixfold at low pressure to seven and eightfold at high pressure fits the trend of the coordination number increasing concomitantly with pressure.[19] One can also note that superconductivity studies on tungsten nitrides are scarce (Figure S1, Supporting Information), with the only demonstrated case being W_2N,[20] which shows a T_c of 1.3 K at ambient conditions, representing only marginal improvement compared to pure tungsten (0.011 K).[21]

From this literature survey, it is clear that the W–N system has yet to be investigated in the mild to moderate pressure regime, namely from ≈20 to 70 GPa. According to theoretical calculations,[22] this pressure domain is promising for the discovery of novel solids with attractive mechanical properties. In the current work, the W–N system was investigated between 35 and 56 GPa and two new tungsten nitrides, W_2N_3 and W_3N_5, were synthesized, along with the known MoC-type $WN_{0.6}$ and WC-type WN.[14d] Their structures, solved and refined by single-crystal X-ray diffraction (SCXRD), are analyzed, and their bulk moduli are determined. The two new solids are also found to be recoverable to ambient conditions and stable in air. The Vickers hardness of W_2N_3 and W_3N_5 is calculated by ab initio methods, as well as their phonon dispersion and electron band structure, superconducting transition temperature, and electron localization function. Signs of the superconducting transition for W_2N_3 at low temperatures have been observed experimentally. The relationship between the crystal structures of these tungsten nitrides and their mechanical and electronic properties is discussed.

2. Results and Discussion

2.1. Synthesis and Data Analysis Procedure

For the performed experiments, three independent experiments with BX90-type DACs equipped with 250 or 200 µm culet anvils were prepared. In two of the experiments, tungsten metal pieces were loaded in the experimental chamber along with high-pressure molecular nitrogen (≈2000 bars), which served as both a reagent and a pressure-transmitting medium (PTM). In the third experiment, $Be_4W_2N_5$, synthesized in a large-volume press, was loaded with neon in the sample chamber. The equation of state (EOS) of tungsten or neon was used to estimate the pressure in the sample chamber.[5,23] The full experimental and calculation details can be found in the Experimental Section. In the

E. L. Bright, S. Gallego-Parra
European Synchrotron Radiation Facility
Grenoble 38000, France
N. Giordano
Photon Science
Deutsches Elektronen-Synchrotron
22607 Hamburg, Germany
Y. Yin, A. Aslandukov, F. I. Akbar
Material Physics and Technology at Extreme Conditions
Laboratory of Crystallography
University of Bayreuth
95447 Bayreuth, Germany
E. Gregoryanz
Center for High-Pressure Science and Technology Advanced Research
Shanghai 201203, P. R. China
E. Gregoryanz
Key Laboratory of Materials Physics
Institute of Solid State Physics
Chinese Academy of Sciences (CAS)
Hefei, Anhui 230031, P. R. China
M. Bykov
Institute of Inorganic and Analytical Chemistry
Johann Wolfgang Goethe Universität
60438 Frankfurt, Germany

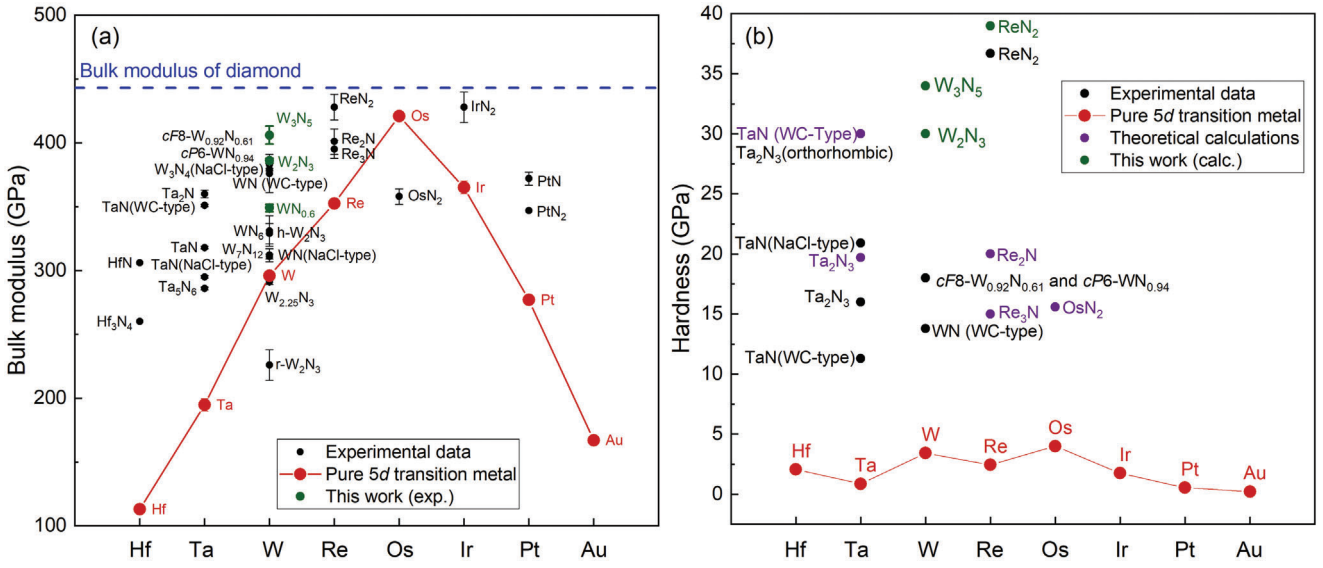

Figure 1. Bulk modulus and hardness of pure 5*d* transition metals and their corresponding nitrides, as reported in the literature[1,2,4–7,14] and this study. The data used to produce these graphs can be found in Table S1 (Supporting Information). a) The experimentally determined bulk modulus of the pure metals and their nitrides is represented by solid red and black dots, respectively. The three synthesized tungsten nitrides reported in this study are indicated by green dots. The horizontal dashed blue line represents the bulk modulus of the diamond.[15] b) The experimentally measured hardness value (exp.) of pure 5*d* transition metals and their nitrides is illustrated by solid red and black dots, respectively. The theoretically calculated hardness (calc.) of metal nitrides found in the literature is shown as purple dots. The predicted Vickers hardness of the two newly synthesized tungsten nitrides and the previously reported ReN_2[2a] are represented by green dots. Only the 5*d* transition metal nitrides stable at ambient conditions are plotted in Figure 1b.

first experiment (exp #1), a sample was initially compressed to 35.0 GPa and laser-heated to 3000(200) K. After laser-heating, an X-ray diffraction map (**Figure 2c**) of the sample revealed the presence of previously absent diffraction spots (Figures S2–S5, Supporting Information), suggesting the formation of a compound. SCXRD measurements performed on the polycrystalline sample resulted in high-quality data from which the structure of the novel W_2N_3 compound was solved and refined (Figures S2,S4, Supporting Information). The presence of MoC-type $WN_{0.6}$ was also found (Table S2, Figure S4, Supporting Information).[4,14d] The sample was then further compressed to 56.0 GPa and laser-heated to 3100(200) K. While the diffraction signal of W_2N_3 was seen, new diffraction spots were also observed (Figures S3,S5, Supporting Information). From the collected single-crystal data, the unidentified diffraction spots could be assigned to the previously unknown W_3N_5 compound, for which a full structure model was obtained (Figure 2). In another independent experiment (exp #2), the pressure was increased to 45 GPa and the sample was laser-heated to 2400(200) K, W_2N_3 and the previously reported WC-type WN was found. In the third experiment (exp #3), with the starting materials $Be_4W_2N_5$ and Ne, the pressure was increased to 40.2 GPa and the sample was laser-heated to a temperature higher than 2000 K. In exp #3, only W_2N_3 was found. The outcome of each experiment is summarized in Table S2 (Supporting Information). The presence of other phases was ruled out through the detailed analysis of the powder X-ray diffraction data (Figures S4,S5, Supporting Information). The synthesized compounds were then decompressed to ambient conditions—under which they were found to persist and to be stable in air. SCXRD data were collected at several pressure points during decompression.

2.2. Crystal Structure at Ambient Conditions

The determined crystal system of $WN_{0.6}$ is hexagonal (space group $P6_3/mmc$, no. 194), and the ambient conditions lattice parameters are $a_0 = b_0 = 2.909(5)$ Å and $c_0 = 10.167(4)$ Å, ($V_0 = 74.52(4)$ Å^3), in excellent agreement with previously reported values.[14d] The lattice parameters at different pressures can be found in Table S3 (Supporting Information).

W_2N_3 crystallizes in the orthorhombic crystal system (Figure 2a) with space group *Pnma* (no. 62). The lattice parameters of W_2N_3 at ambient and high pressure can be found in Table S4 (Supporting Information), while the refinement results, quality factors and crystal structure at ambient condition and 35.0 GPa can be found in Tables S6–S8 (Supporting Information). The CIF (Crystallographic Information File) files at ambient condition and 35.0 GPa are deposited in the Cambridge Crystallographic Data Center (CCDC) with the deposition numbers 2305422 and 2305423, respectively. W_2N_3 is isostructural to the previously reported transition metal nitrides η-Ta_2N_3[14] and Nb_2N_3[24] and has the U_2S_3-type structure. Furthermore, the existence of W_2N_3 was predicted by previous theoretical calculations.[22a] The crystal structure of W_2N_3 (Figure 2a) is composed of two crystallographically distinct tungsten atoms (W1 and W2) as well as the three unique nitrogen atoms (N1, N2 and N3), all located on the 4*c* Wyckoff position. Each tungsten atom is surrounded by seven nitrogen atoms, forming WN_7 polyhedra. For the $W1N_7$ polyhedron, it is edge-sharing with five $W2N_7$ and two $W1N_7$ polyhedra, as well as face-sharing with two $W1N_7$ polyhedra along the *b*-axis (Figure 2b). For the $W2N_7$ polyhedron, it is edge-sharing with five $W1N_7$ and four $W2N_7$ polyhedra. At ambient conditions, the W—N bond distance in

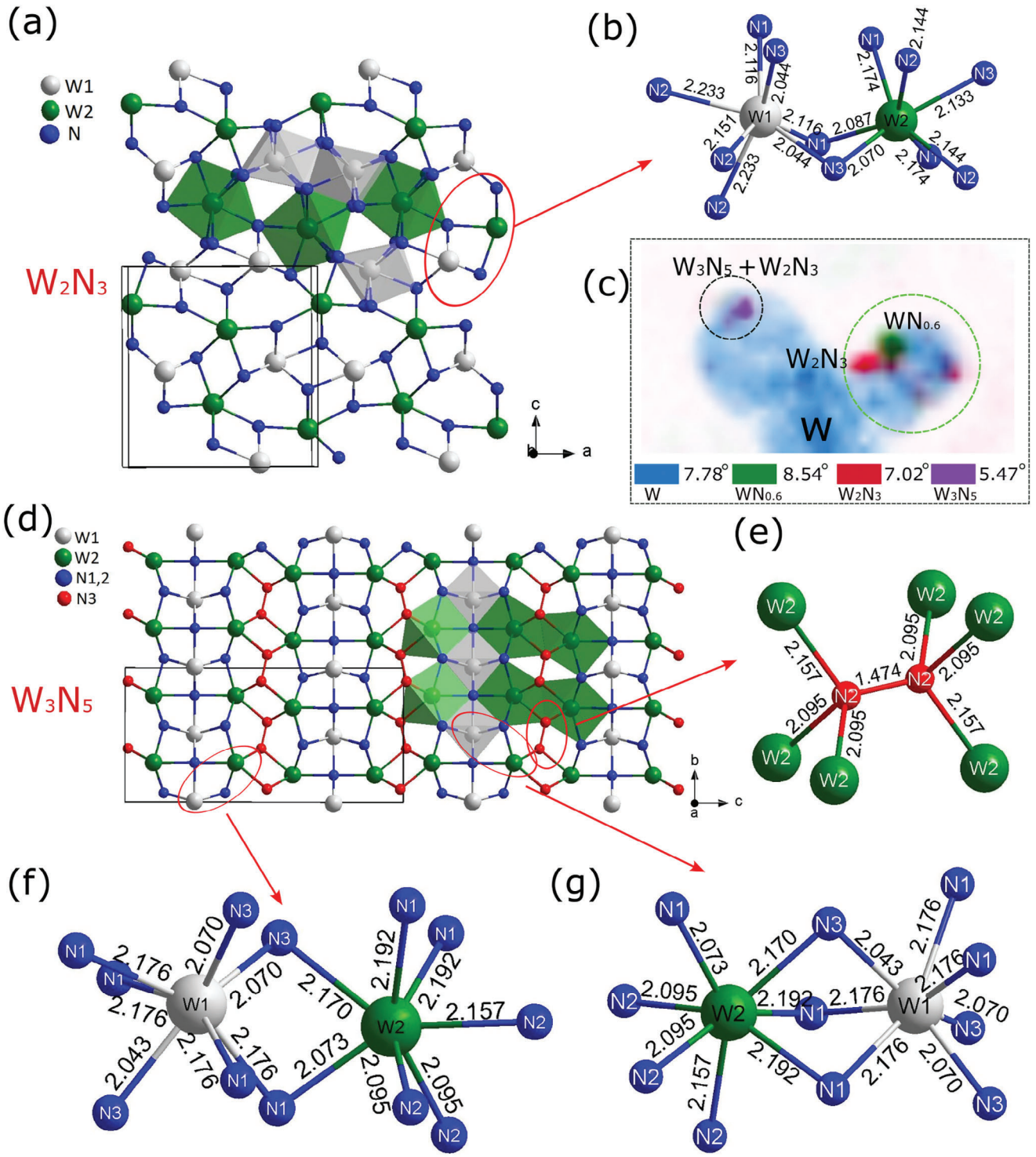

Figure 2. Crystal structure of the two new tungsten nitrides at ambient conditions. a) Crystal structure of W_2N_3. b) Edge-sharing WN_7 polyhedra found in the crystal structure of W_2N_3. c) X-ray diffraction map of the sample cavity in exp#1 at 56 GPa, showing the position of tungsten (sky blue), W_2N_3 (red), W_3N_5 (pink), and $WN_{0.6}$ (green). The green and black circles indicate the laser-heated position at 35 and 56 GPa, respectively. The intensity of the peak at the 2θ angle provided for each compound was utilized to construct the map. d) Crystal structure of W_3N_5; the discrete N^{3-} anions are shown in blue while the $(N_2)^{4-}$ dimers are shown in red. e) The immediate chemical environment of the single bonded nitrogen dimer. f) Edge- and g) face-sharing WN_7 polyhedra found in the crystal structure of W_3N_5. In all cases, the W1 and W2 atoms, crystallographically distinct in both structures, are shown as white and green balls. The bond distances indicated next to the bonds are in Å. Unit cells are drawn with continuous black lines.

both distinct WN_7 polyhedra varies from 2.044(3) to 2.233(4) Å, consistent with the W—N bond distance reported in the literature for tungsten nitrides.[4,14a,d,e,h] The W–W distance is 2.9245(3) Å, larger than that of pure tungsten (2.74 Å).[14r] The discrete nitrogen atoms are four (N3) or fivefold (N1, N2) coordinated by tungsten.

W_3N_5 contains both discrete N atoms and N_2 dimers—and can thereby also be written as $W_3(N_2)(N)_3$—and crystallizes in the orthorhombic crystal system (Figure 2d), adopting space group *Cmcm* (no. 63). The lattice parameters of W_3N_5 at ambient and at high pressure can be found in Table S5 (Supporting Information), while the refinement results, quality factors and crystal structure at ambient conditions and 56.0 GPa can be found in Tables S9–S11 (Supporting Information). The deposition number of the CIF files in CCDC at ambient conditions and 56.0 GPa are 2305424 and 2305425, respectively. W_3N_5 has two crystallographically distinct tungsten atoms on the 4*c* (W1) and 8*f* (W2) Wyckoff positions. The discrete N atoms (N1 and N3), which usually exhibit an -III oxidation state, can thus be written as N^{3-} anions, and are located on 4c and 8*f* Wyckoff sites, and the N2 atoms (8*f* Wyckoff site) form N_2 dimers. The bond length of the N_2 dimer is found to be 1.47(3) Å at ambient conditions, suggesting a single bond and thus a N_2^{4-} pernitride,[25] consistent with that found in Mo_3N_5 (1.412 Å),[26] PtN_2 (1.42 Å),[27] OsN_2 (1.40 Å),[27] IrN_2 (1.42 Å),[27] and ReN_2 (1.412 Å).[2a] The nitrogen atoms constituting the N_2 dimers are bonded to three tungsten atoms at a distance of 2.095(8) or 2.157(12) Å (Figure 2e). The discrete N^{3-} anions have five tungsten atoms in their first coordination shell, each W1 atom is surrounded exclusively by seven discrete N^{3-} anions while each W2 atom is surrounded by four discrete N^{3-} anions plus three pernitride N_2^{4-} anions, producing WN_7 polyhedra. Each $W1N_7$ polyhedra is face-sharing with two $W2N_7$ polyhedra plus two $W1N_7$ polyhedra, and edge-sharing with four $W2N_7$ polyhedra (Figure 2f,g). In sum, the crystal structure could be described as columns of $W1N_7$ polyhedra running along the *b*-axis, separated by columns of pairs of edge-sharing $W2N_7$ polyhedra, interconnected through N_2 dimers (Figure 2d). The W—N bond distance ranges from 2.043(15) to 2.176(8) Å, very similar to those found in W_2N_3. W_3N_5 is isostructural to the recently discovered Mo_3N_5,[26] a fact that is easily rationalized given that molybdenum is the lighter homolog of tungsten in the periodic table.

2.3. Atomic Charge and Bond Type

Based on the chemical formula of W_2N_3 and under a fully ionic approximation, where all nitrogen atoms are considered as forming nitrides (N^{3-}), it is reasonable to assume that the W atoms share a combined charge of +9. Under this assumption, one tungsten would be in the oxidation state of +V and the other in +IV. This assignment is supported by smaller volumes of $W1N_7$ polyhedra compared to $W2N_7$ (Figure 4e). In the case of W_3N_5, given the $W_3(N_2)^{4-}(N^{3-})_3$ chemical formula, the three discrete N^{3-} anions and one N_2^{4-} collectively carry a charge of −13. Consequently, a plausible charge distribution across the two distinct tungsten atoms would entail W2 (8*f* Wyckoff site) to have a +4 charge and W1 (4*c* Wyckoff site) a +5 charge. To better understand the bond character and charge distribution in these W–N solids, Löwdin charge, Mulliken charge, and integrated crystal orbital bond index (ICOBI) were calculated (Tables S12–S14, Supporting Information). The calculated Mulliken charge for tungsten in those two new compounds fall within the range of +1.33 *e* to +1.43 *e*. For the discrete N^{3-} anion, the calculated charge varies from −0.89 *e* to −0.97 *e*, and for the N_2^{4-} pernitride, the charge is −1.2 *e*. The significantly lower charges for all the cations and anions compared to the oxidation states suggest that the bonds are far from being purely ionic. The bond covalency was assessed through the ICOBI. The ICOBI value for the W—N bonds fall within the range of 0.53 to 0.72 in the case of W_3N_5, indicating a substantial electron contribution from covalent bonding. This suggests that the bond between these atoms is a mixture of ionic and covalent. This observation aligns with the ICOBI versus absolute electronegativities difference relationship established for some compounds.[28] In that relationship, the ICOBI for the classical ionic compound NaCl is 0.09, indicating a negligible contribution from the covalent bond. Conversely, the calculated ICOBI for the classical covalent bond compound diamond is 0.95. The ICOBI calculated for the N_2 pernitride is 0.98, implying a single-bond, in agreement with the deduction made from the N—N bond length. This analysis is further supported by the calculated electron localization function (ELF) values obtained for different W—N bonds and the N—N dimer (Figures S6,S7, Supporting Information). The ELF value at the bond critical point of the W—N bond hovers ≈0.5; an ELF of 0.5 corresponds to electron-gas-like pair probability,[29] and the value at the bond critical point for the N—N dimer is as high as 0.8, a value commonly observed for classical covalent bonds.[30]

2.4. Superconductivity, Phonons, and Electronic Properties

The vibrational and electronic properties of the newly synthesized tungsten nitrides have been explored through theoretical calculations employing density functional theory (DFT). This investigation included phonon and electronic band structures (**Figure 3**; Figures S8,S9, Supporting Information) as well as elastic constants (Table S15, Supporting Information) at ambient pressure. The phonon band structure of both compounds exhibited no negative frequencies, thereby confirming their dynamical stability. The phonon band structure of W_2N_3 (Figure 3a) can be divided into two regions. The low-frequency region, below 10 THz, features contributions from tungsten atoms. The middle-frequency region between 10 to 25 THz displays the contribution from the discrete N^{3-} nitrogen alone. The phonon band structure of W_3N_5 (Figure 3b) can be divided into three regions and, besides two regions analogous to those in W_2N_3, it has a high-frequency region (>25 THz) with the sole contributor being the single-bonded N—N dimer. The peak of the latter vibration band is at a frequency of 27 THz (≈934 cm^{-1}), which closely mirrors the calculated peaks in other pernitrides, such as PtN_2 (752 cm^{-1}),[31] IrN_2 (836 cm^{-1}),[31] OsN_2 (778 cm^{-1}),[31] and ReN_2 (1031 cm^{-1}),[2a] yet notably differs from the vibrational frequency of the N=N double bond as seen in N_2H_2 (1550 cm^{-1}).[32]

The electronic band structures of W_2N_3 and W_3N_5, as depicted in Figures S8 and S9 (Supporting Information) respectively, reveal their closed band gap and therefore their metallic nature. The T_c of those two compounds has been estimated using the

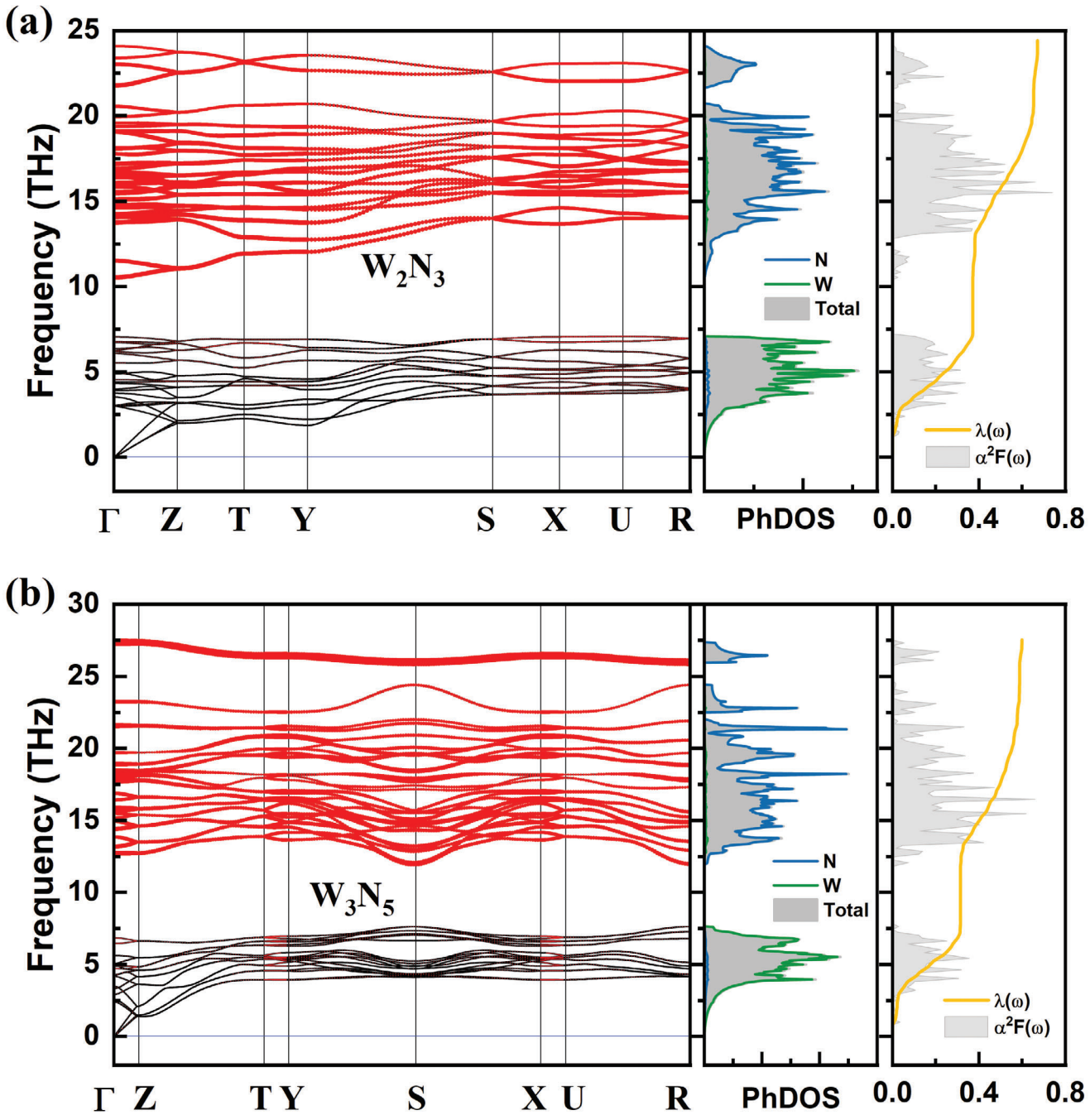

Figure 3. Density functional theory calculated phonon dispersion weighted by the magnitude of the phonon linewidth (red dots), projected phonon density of states and Eliashberg spectral function $\alpha^2F(\omega)$ (grey), as well as the integrated strength of electron–phonon coupling of $\lambda(\omega)$ (yellow lines) for a) W_2N_3 and b) W_3N_5 at ambient pressure. The density of the red dots gives rise to the appearance of lines with varying broadness.

Allen–Dynes-modified McMillan formula, as shown in the Section Density Functional Theory Calculations.[33] The T_c values for W_2N_3 and W_3N_5 at ambient pressure are found to be 11.6 and 9.4 K, respectively. In this formula, the T_c is directly correlated with the electron–phonon coupling (EPC) parameter $\lambda(\omega)$ (0.67 and 0.60 calculated for W_2N_3 and W_3N_5, respectively) and the logarithmic average frequency ω_{log} (369.2 and 397.2, calculated for W_2N_3 and W_3N_5, respectively). $\lambda(\omega)$ is obtained by integrating the Eliashberg spectral function $\alpha^2F(\omega)/\omega$ over the entire frequency range, and ω_{log} is calculated by integrating the $\alpha^2F(\omega)\cdot\ln\omega/\omega$, where the Eliashberg spectral function $\alpha^2F(\omega)$ in different frequency regions is represented by the grey area in Figure 3. In the low-frequency region of the phonon dispersion, the tungsten atoms contribute 56.6% and 52.4% to the total integration of λ in W_2N_3 and W_3N_5, respectively. Another significant contribution to λ comes from the middle-frequency region, indicating the

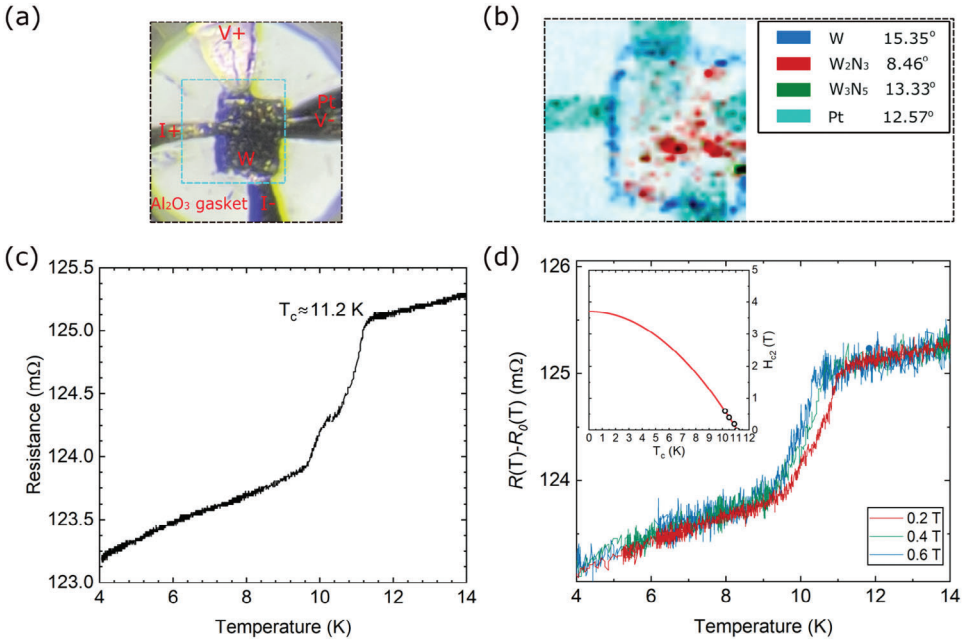

Figure 4. Transport measurements for a laser-heated W–N_2 sample at 50 GPa. a) An optical image of the sample after laser heating at 50 GPa. The aqua-colored square surrounding the initially pure tungsten sample shows the boundary of the X-ray diffraction map shown in (b). b) The X-ray diffraction intensity map obtained at 50 GPa displays the positions of tungsten (sky blue), W_2N_3 (red), W_3N_5 (green), and Pt (aqua). The intensity of the peak at the 2θ angle provided for each compound was utilized to construct the map. For clarity, nitrogen, present in both the ι- and ε-phases, was omitted from the map, as it was found essentially everywhere in the sample chamber. c) Electrical resistance as a function of temperature measured after laser heating tungsten. d) Electrical resistance as a function of the temperature of the synthesized sample under an applied magnetic field up to 0.6 T. The insert displays the superconducting upper critical field (H_{c2}) versus the critical temperature (T_c), fitted with Ginzburg–Landau (GL) formalisms.[37]

vibration of the discrete N^{3-} anions, contributing 43.4% and 45.6% of the total integration of λ in W_2N_3 and W_3N_5, respectively. The presence of nitrogen is hence responsible for the increased T_c compared to that of pure tungsten. The N—N dimer in W_3N_5 contributes only 2% to λ and thus has a negligible impact on the T_c of W_3N_5. The T_c predicted for W_2N_3 and W_3N_5 at ambient conditions also significantly exceeds that of pure tungsten (0.011 K), as well as those of other 5*d*-transition metal nitrides, such as HfN (8.83 K),[34] and cubic-TaN (6.5 or 8.15 K)[35] (Figure S1, Supporting Information). Notably, W_2N_3 exhibits the highest T_c among all reported 5*d*-transition metal nitrides to date (Figure S1, Supporting Information) and is comparable to the highest T_c, 16 K of δ-NbN,[36] found among all the transition metal nitrides. Following the same methodology, the T_c of W_2N_3 and W_3N_5 was calculated at 50 GPa (Figure S10, Supporting Information). The estimated T_c values for W_2N_3 and W_3N_5 are 9.8 and 7.2 K, respectively.

An independent cell (exp #4) has been prepared to measure the transport properties of the synthesized sample at 50 GPa (**Figure** 4a). An X-ray diffraction mapping (Figure 4b) was conducted on the same sample at 50 GPa. An example of the Le Bail refinement of the powder X-ray diffraction data obtained from the center position in the map is shown in Figure S11 (Supporting Information). The map reveals the synthesized sample to be predominantly composed of W_2N_3 (in red) with a small proportion of W_3N_5 (in green), along with ι- and ε-nitrogen, and pure tungsten (in blue). The resistance measurements of the synthesized sample (Figure 4c) exhibit an abrupt drop at a temperature of 11.2 K. This can be interpreted as the signature of a superconducting transition in W_2N_3 since it is the primary compound in the sample chamber and because the T_c for pure tungsten is known to be significantly below 11 K,[21] while both ι- and ε-nitrogen are insulators. The resistance does not decrease to zero due to the sample's inhomogeneity and the lack of a full W_2N_3 conduction path between the electrodes. Further evidence pointing to a superconducting behavior is observed in the decrease of T_c under an applied magnetic field (Figure 4d). Fitting and extrapolation of the upper critical field (H_{c2}) versus temperature suggest that the T_c will be completely suppressed at an H_{c2} higher than 3.7 T. The experimentally measured T_c of 11.2 K matches very well with the value expected from DFT calculations at 50 GPa, that is, 9.8 K.

2.5. Compressibility and Hardness

The structures of W_2N_3 and W_3N_5 were refined at each pressure step during the decompression, and the obtained unit cell volumes were plotted in **Figure** 5a,b. The data was fitted using a second-order Birch–Murnaghan (BM) EOS,[38] and the quality of the fitting was evaluated through the Eulerian strain (*f*) versus the normalized pressure (F) plot (Figures S12,S13, Supporting Information). The bulk modulus of W_2N_3 and W_3N_5 was determined to be 380(3) and 406(7) GPa, respectively. As both values are above the 300 GPa threshold, they qualify as ultra-incompressible.[39] As depicted in Figure 1a, their bulk modulus is higher than those of any previously reported tungsten nitrides. Figure 5d illustrates the pressure dependence of the normalized lattice parameters of W_3N_5. The crystal exhibits an isotropic

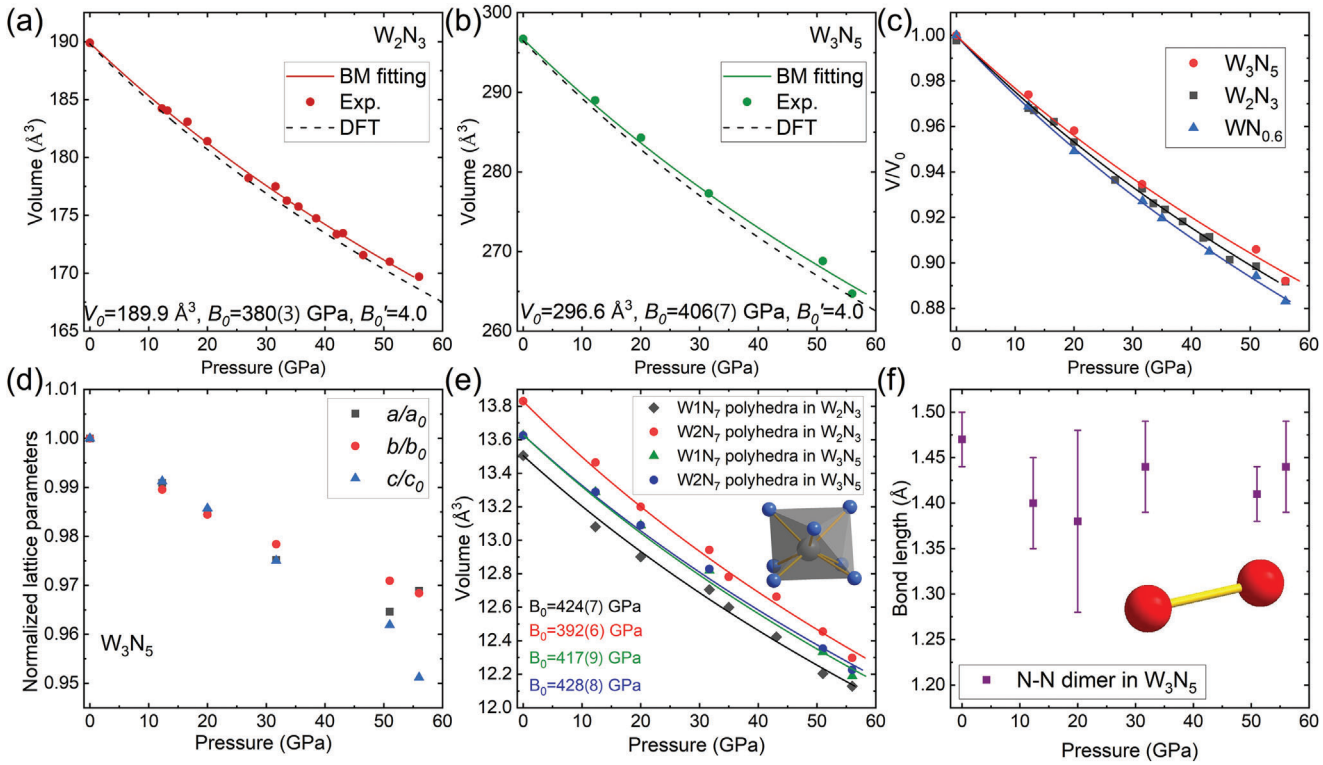

Figure 5. Physical properties of W_2N_3 and W_3N_5 extracted from the SCXRD data solution and refinement. Dots are experimental data and solid lines are second-order BM equations of state fits. a) Unit cell volume of W_2N_3 as a function of pressure (Exp.). b) Unit cell volume of W_3N_5 as a function of pressure (Exp.). The dashed lines are the theoretically calculated equation of state (DFT). c) Normalized unit cell volume of $WN_{0.6}$ (blue triangles), W_2N_3 (black squares), and W_3N_5 (red circles) as a function of pressure. d) Normalized lattice parameters for W_3N_5 at different pressures. e) The green/blue and red/black dots are the volume of the WN_7 polyhedra extracted from W_3N_5 and W_2N_3, respectively. The same color system was also applied to the WN_7 bulk modulus values written in the figure. The inset of this graph is a representative WN_7 polyhedra ($W1N_7$ in W_3N_5 at ambient conditions), in which the tungsten and nitrogen atoms are shown by grey and blue balls. f) Pressure dependence of the bond distance of the N—N dimer.

compressibility at lower pressures and minor anisotropic behavior at higher pressures, with the *b*-axis becoming the most incompressible axis. This anisotropy is attributed to the orientation of the N—N dimer, which is almost fully parallel to the *b*-axis. The bond length of this N—N dimer remains nearly unchanged under compression, as shown in Figure 5f. The observed anisotropic behavior is unrelated to the arrangement of the WN_7 polyhedra, as the mixture of edge- and face-sharing connected WN_7 polyhedra are observed along all three crystallographic directions. The bulk modulus of $WN_{0.6}$ was also determined (356(2) GPa, see Figure 5c; Figure S14, Supporting Information) and found to be slightly larger than the literature value (338(3) GPa).[14d]

To shed some light on the underlying mechanism behind the incompressibility of W_2N_3 and W_3N_5, the pressure versus volume relationship of their WN_7 polyhedra was plotted (Figure 5e). A second-order BM EOS was employed to fit the volume of the polyhedra. The bulk moduli of all four distinct WN_7 are found to be closely related, with values of 424(7) GPa (392(6) GPa) for the $W1N_7$ ($W2N_7$) polyhedra in W_2N_3 and 417(9) GPa (428(8) GPa) for the $W1N_7$ ($W2N_7$) polyhedra in W_3N_5. It appears clear the bulk moduli value of the W_2N_3 and W_3N_5 compounds are similar to that of their constituting WN_7 unit. As such, it can be inferred that the compounds' bulk moduli mainly originate from the compressibility of the WN_7 polyhedra themselves. Indeed, the polyhedra linkages are not thought to significantly affect the solids' compressibility, as face- and edge-sharing—both exclusively present in W_2N_3 and W_3N_5 and along all three crystallographic directions—are the most rigid.[40] The mild difference in compressibility between W_2N_3 and W_3N_5 is likely due to the existence of the ultra-incompressible N—N dimer in W_3N_5 (Figure 5f). This dimer strengthens the gaps between pairs of $W2N_7$ polyhedra through the substantial Coulomb interaction between the paired nitrogen atoms,[41] as also found in IrN_2,[1,31] PtN_2,[14p,31] and ReN_2.[2a]

The theoretical calculations of the mechanical properties, including elastic constant, bulk modulus, shear modulus, Young's modulus, and Vickers hardness, of the two new tungsten nitrides as well as for ReN_2, can be found in Table S15 (Supporting Information). In comparison to the hardness of 5*d* transition metal nitrides (and the pure metals) summarized in Figure 1b, both of the reported tungsten nitrides exhibit significantly higher hardness values compared to the tungsten nitrides reported in the literature, with their calculated Vickers hardness being of 30 and 34 GPa for W_2N_3 and W_3N_5, respectively. It is noteworthy that the calculated Vickers hardness for both W_2N_3 and W_3N_5 is comparable to the reported nanoindentation hardness (36.7 GPa) of ReN_2,[2a] which is well reproduced by our calculations (39 GPa, see Table S15, Supporting Information). The agreement

observed between the calculated Vickers hardness and the experimental hardness for ReN_2 underlines the reliability of this hardness model for the two new tungsten nitrides presented in this study. According to the assumptions made by Gao et al.,[42] the hardness of a covalent crystal can be described by the resistance of the bond against the external forces per unit area.[43] Therefore, the high Vickers hardness found in W_2N_3 and W_3N_5 could be attributed to the higher covalency of the W—N bonds within the WN_7 polyhedra. Additionally, the existence of the N—N dimer and the strong covalent bond between them contribute to the even greater hardness found in W_3N_5 and ReN_2.

3. Conclusion

By employing a combination of single-crystal X-ray diffraction techniques and theoretical calculations, we have successfully characterized two novel tungsten nitrides, synthesized at high pressure and temperature and recovered to ambient conditions, namely W_2N_3 and W_3N_5. Both compounds' mechanical stability at ambient pressure has been confirmed theoretically. W_2N_3, for which the lowest synthesis conditions found in this work are 35 GPa and 3000(200) K, exhibits a bulk modulus of 380(3) GPa, a calculated Vickers hardness of 30 GPa and is calculated to be superconducting below 11.6 K at ambient pressure and 9.8 K at a pressure of 50 GPa. Transport measurements suggest W_2N_3 to feature, at 50 GPa, a superconducting transition at 11.2 K. Notably, its critical temperature (T_c) predicted at ambient pressure is the highest among 5*d*-transition metal nitrides reported to date.

W_3N_5, comprised of both isolated N^{3-} as well as N_2^{4-} anions, is formed at a pressure of 56 GPa and a temperature of 3100(200) K, and has a bulk modulus of 406(7) GPa, a calculated Vickers hardness of 34 GPa and a superconducting transition temperature of 9.4 K at ambient pressure and 7.2 K at 50 GPa. Remarkably, its bulk modulus stands as the highest within the tungsten–nitrogen system, comparable to the most incompressible 5*d* transition metal nitrides.

The exceptionally incompressible behavior exhibited by both compounds can be attributed to the interconnected face- and edge-sharing WN_7 polyhedra. Additionally, the presence of the N_2 dimer in W_3N_5 contributes to its exceptional mechanical properties. Electronic band structure calculations indicate a closed band gap for both compounds, indicative of their metallic nature. The competitive hardness of these two compounds, coupled with the significantly lower cost of tungsten compared to other 5*d* transition metals, positions them as excellent candidates for industrial applications requiring toughness, good electronic conductivity, and cost-effective materials.

4. Experimental Section

High-Pressure Experiments: Three independent series of experiments were performed for the synthesis of tungsten nitrides by using BX90-type DACs with Boehler–Almax type diamonds. The synthesis conditions and the outcomes are summarized in Table S2 (Supporting Information). Experiment #1 (exp #1) was conducted in a DAC equipped with a pair of 250 µm-culet diamonds, while exp #2 and #3 were conducted in DACs equipped with a pair of 200 µm-culet diamonds. A rhenium foil was used as the gasket and pre-indented to a thickness of 25 µm. A 120-µm hole was drilled in the center of the indentation and served as the sample chamber. In exp #1 and #2, several pieces of high-purity tungsten (Alfa Aesar, purity 99.9%) were loaded in the sample chamber with molecular nitrogen, the latter serving as both a reagent and a PTM. In exp #3, the ternary precursor $Be_4W_2N_5$, synthesized in a large volume press was used. The crystal structure and synthesis details of the precursor would be reported elsewhere. This sample was loaded with neon. The samples were compressed to the target pressure of 35 and 56 GPa in exp #1, 45 GPa in exp #2, and 40 GPa in exp #3, respectively. Then the starting materials were laser heated with a home-built double-sided YAG laser-heating system. The temperature was measured by using the sample's thermal radiation. The pressure in the sample chamber was determined either from the EOS of tungsten (exp #1 and #2)[5] or Ne (exp #3).[23] Transport measurements (exp #4) were performed using a symmetric-type steel DAC suitable for electrical measurements in low-applied magnetic fields. This cell employed an insulating Al_2O_3-epoxy composite gasket in order to electrically insulate the electrodes from the metallic gasket. To provide the electrical connection to the sample, four Pt wires were placed in the sample chamber and fixed in place with silver epoxy before loading the W foil (99.999%, Goodfellow) and the research-grade nitrogen (99.9995%) at 2 kbar, the latter which acted as both the reactant and a hydrostatic PTM. After compression to 50 GPa (determined using the Raman shift of the diamond peak) the W foil was laser heated to a temperature of ≈2300 K.

X-Ray Diffraction Experiments: SCXRD experiments were performed at the ID11 beamline of the European Synchrotron Radiation Facility[44] (ESRF, in Grenoble, France), the P02.2 beamline of PETRAIII[45] (in Hamburg, Germany) synchrotron and 13IDD beamline of the APS (in Chicago, United States). At the ID11 beamline of the ESRF, the wavelength of the monochromatic X-ray beam was 0.2846 Å, the beam spot size was ≈1 × 1 µm^2 (full width at half maximum), and a Dectris Eiger2 X CdTe 4M detector was used to collect the signal. At the P02.2 beamline of PETRAIII, the wavelength of the monochromatic X-ray beam was 0.2905 Å, the beam spot size was ≈2 × 2 µm^2, and a Perkin Elmer XRD 1621 detector was used to collect the signal. At the 13IDD beamline of APS, the wavelength of the monochromatic X-ray beam was 0.2952 Å, and a Pilatus CdTe 1M detector was used to collect the signal. In all the cases, an X-ray mapping was performed in the sample chamber around the heated area to find the position of interest for SCXRD data collection, then obtained by rotating the cell around the vertical ω-axis in steps of 0.5 degrees from −36° to +36° (exp #1), or −30° to +30° (exp #2 and #3) for DACs with a smaller opening. The X-ray diffraction map of the sample in exp #4 was collected at the ID15B beamline of the ESRF. The wavelength of the monochromatic X-ray beam was 0.4094 Å, the beam spot size was ≈1 × 1 µm^2 (full width at half maximum), and a Dectris Eiger2 X CdTe 9M detector was used to collect the signal.

The CrysAlis^{Pro} software[46] package was used for the SCXRD data analysis, including peak search, removing the parasitic peak from the diamond anvils, unit cell determination, and data integration. An orthoenstatite single crystal ($(Mg_{1.93}Fe_{0.06})(Si_{1.93}, Al_{0.06})O_6$, space group: *Pbca*, lattice parameter: a = 8.8117(2) Å, b = 5.1832(1) Å, c = 18.2391(3) Å) was used to calibrate the instrumental model used in CrysAlis^{Pro}, which included the sample-to-detector distance, the detector's origin, offsets of goniometer angles, and the rotation of both the X-ray beam and the detector with respect to the instrument axis. The DAFi program[47] was employed to search for the reflections that belonged to an individual single crystal. The crystal structures were solved with the SHELXT structure solution program[48] and refined in the Olex2 software.[49] Powder X-ray diffraction (PXRD) patterns were collected without the rotation of the cell, and integrated to a 2D X-ray diffraction pattern in the DIOPTAS software.[50] The Le Bail refinement of the integrated PXRD spectra was performed in the FULLPROF suite.[51]

Density Functional Theory Calculations: Kohn–Sham DFT-based electronic structure calculations were performed with the QUANTUM ESPRESSO (QE) package[52] using the projector augmented wave method.[53] The generalized gradient approximation by Perdew–Burke–Ernzerhof (PBE) was used for exchange and correlation,[54] the corresponding potential files for W 4*f* electrons and N 1*s* electrons were treated as scalar-relativistic core states. D3 van der Waals (vdW) corrections were included following the approach by Grimme et al.[55] as implemented in

QE for all calculations, except for the estimation of the critical superconducting temperature (see below). Convergence tests with a threshold of 1 meV per atom in energy and 0.1 meV Å^{-1} per atom for forces led to a Monkhorst–Pack[56] ***k***-point grid of 6 × 16 × 5 for W_2N_3 and 22 × 22 × 6 for W_3N_5 with a cutoff for the wave-function expansion of 100 Ry for both phases, with a mild Gaussian smearing of 0.005 Ry. The influence of spin-orbit coupling on the band structure and electronic density of states (Figures S8,S9, Supporting Information), which is in agreement with previous calculations in the W–N system was investigated.[57] Therefore, spin-orbit interactions were not included in further calculations.

Variable cell relaxations (lattice parameters and atomic positions) were performed on all experimental structures to optimize the atomic coordinates and the cell vectors until the total forces were smaller than 0.1 meV Å^{-1} per atom and the deviation from the experimental pressure was below 0.1 GPa. EOS calculations were performed via variable-cell structural relaxations in 5 GPa steps up to 60 GPa. A second-order BM EOS was fitted to the energy–volume points, $P(V)$ calculated, and benchmarked versus the target pressure of the relaxations to ensure convergence. Values of $V_0 = 189.81$ Å^3, $B_0 = 364$ GPa for W_2N_3, and $V_0 = 296.59$ Å^3 and $B_0 = 387$ GPa for W_3N_5 were found, close to the respective values for the bulk modulus of 365 and 385 GPa from elastic constants calculations (see Table S15, Supporting Information). Overall the best agreement with the experiment was found using the PBE functional with vdW corrections.

Löwding and Mulliken charges, as well as the ICOBI, were calculated with the LOBSTER package.[58]

To estimate the "polycrystalline" or Vickers hardness[59] of W_2N_3 and W_3N_5, the single-crystal elastic stiffness constants C_{ij} was calculated and derived the polycrystalline bulk (B_0) and shear (G) moduli. The energy–strain relationships and a finite difference method with (+/−) 1 and 2% strain were utilized and the total energies were calculated using QE with the same numerical parameters as listed above. The values for the elastic constants and moduli can be found in Table S15 (Supporting Information).

Phonon dispersion relations were calculated with Phonopy[60] in a 2 × 4 × 2 and 3 × 3 × 2 supercells for W_2N_3 and W_3N_5, respectively, with ***k***-points adjusted according to the supercell size. Calculations were performed with and without vdW corrections (structures without vdW corrections were re-relaxed to 0 GPa within this level of approximation) to ensure that the T_c calculations in using QE, where vdW corrections cannot be included, adequately represent the phonon dispersion relation. A very small influence was seen and concluded that vdW interactions should not have any significant influence on the calculated transition temperatures.

To estimate T_c, additional phonon and EPC calculations were carried out using density functional perturbation theory[61] as implemented in the QE, the same projected augmented wave pseudopotentials for N and W with a reduced kinetic energy cutoff of 100 Ry were employed. 3 × 5 × 3 and 4 × 4 × 3 ***q***-point grids were employed to calculate the EPC of W_2N_3 and W_3N_5, respectively. Commensurate Monkhorst–Pack grids of 12 × 20 × 12 and 16 × 16 × 12 were used to ensure ***k***-point sampling convergence and Gaussian smearing with a width of 0.01 Ry improving convergence. The superconducting critical temperature T_c was estimated based on the Allen–Dynes modified McMillan formula:[33]

$$T_c = \frac{\omega_{log}}{1.2} \exp\left[-\frac{1.04\,(1+\lambda)}{\lambda - \mu^* - 0.32\lambda\mu^*}\right] \quad (1)$$

where μ* is the effective Coulomb pseudopotential which was set to a typical value of 0.1. The integrated EPC constant can be evaluated by

$$\lambda\ (\omega) = \int_0^{\omega} \frac{\alpha^2 F\,(\omega')}{\omega'} d\omega' \quad (2)$$

The EPC constant λ used in Equation (1) is $\lambda\ (\omega_{max})$, where ω_{max} is the maximum of the phonon frequency.

Here, ω_{log} is the logarithmically averaged characteristic phonon frequency, which is defined as

$$\omega_{log} = \exp\left[\frac{2}{\lambda} \int \frac{d\omega}{\omega} \alpha^2 F\,(\omega) \ln \omega\right] \quad (3)$$

Transport Measurements: Four-probe electrical measurements were performed using a Keithley 6221 current source combined with a Stanford SR830 Lock-In amplifier for voltage measurements, with a 141 μA excitation current at 84 Hz. Due to the large mass of the cell, data was taken at an approximate rate of 0.1–0.2 K min^{-1} to ensure good thermalization. For the electrical measurements in an applied magnetic field, resistance offsets were applied to normalize the data above the superconducting transition to remove the effects of any observed magnetoresistance. T_c was extracted as the temperature at 80% of the observed resistance drop.

Supporting Information

Supporting Information is available from the Wiley Online Library or from the author.

Acknowledgements

The authors acknowledge the European Synchrotron Radiation Facility (ESRF), the Deutsches Elektronen-Synchrotron (DESY), and Advanced Photon Source (APS), Argonne National Laboratory for the provision of beamtime at the ID11, ID15B, P02.2, and 13IDD beamlines, respectively. D.L. thanks the UKRI Future Leaders Fellowship (MR/V025724/1) for financial support. M.B. acknowledges the support of Deutsche Forschungsgemeinschaft (DFG Emmy-Noether project BY112/2-1). G.K. thanks the Friedrich Naumann Foundation for Freedom for a Ph.D. scholarship with Funds from the Federal Ministry of Education and Research (BMBF). B.M. and R.S.M. acknowledge the European Research Council (ERC) under the European Union's Horizon 2020 research and innovation program (Grant Agreement No. 101002868). Portions of this work were performed at GeoSoilEnviroCARS (University of Chicago, Sector 13), GeoSoilEnviroCARS was supported by the National Science Foundation – Earth Sciences (EAR-1634415). This research used resources from the Advanced Photon Source, a U.S. Department of Energy (DOE) Office of Science User Facility operated for the DOE Office of Science by Argonne National Laboratory under Contract No. DE-AC02-06CH11357. F.T. acknowledge support from the Knut and Alice Wallenberg Foundation (Wallenberg Scholar grant no. KAW-2018.0194). I.O. and M.P.A. thank UKRI Future Leaders fellowship Mrc-Mr/T043733/1 for the financial support. L.-T.S. acknowledges the Guangdong Basic and Applied Basic Research Foundation (Grant No. 2022a1515110404). Computations were enabled by resources provided by the National Academic Infrastructure for Supercomputing in Sweden (NAISS) and the Swedish National Infrastructure for Computing (SNIC) using Dardel at the PDC Center for High-Performance Computing, KTH Royal Institute of Technology and LUMI at the IT Center for Science (CSC), Finland partially funded by the Swedish Research Council through grant agreements no. 2022–06725 and no. 2018—05973. For the purpose of open access, the author had applied a Creative Commons Attribution (CC BY) license to any Author Accepted Manuscript version arising from this submission.

Conflict of Interest

The authors declare no conflict of interest.

Data Availability Statement

The data that support the findings of this study are available from the corresponding author upon reasonable request.

Keywords

high hardness, high-pressure synthesis, single-crystal X-ray diffraction, tungsten nitrides, ultra-incompressible

Received: November 5, 2023
Revised: April 29, 2024
Published online: May 15, 2024

[1] A. F. Young, C. Sanloup, E. Gregoryanz, S. Scandolo, R. J. Hemley, H. K. Mao, *Phys. Rev. Lett.* **2006**, *96*, 155501.
[2] a) M. Bykov, S. Chariton, H. Fei, T. Fedotenko, G. Aprilis, A. V. Ponomareva, F. Tasnadi, I. A. Abrikosov, B. Merle, P. Feldner, S. Vogel, W. Schnick, V. B. Prakapenka, E. Greenberg, M. Hanfland, A. Pakhomova, H. P. Liermann, T. Katsura, N. Dubrovinskaia, L. Dubrovinsky, *Nat. Commun.* **2019**, *10*, 2994; b) A. L. Ivanovskii, *Inorg. Mater., Appl. Res.* **2012**, *3*, 319.
[3] C. Geibel, H. Rietschel, A. Junod, M. Pelizzone, J. Muller, *J. Phys. F: Met. Phys.* **1984**, *15*, 405.
[4] C. C. Chang, T. Sasaki, N. A. Gaida, K. Niwa, M. Hasegawa, *Inorg. Chem.* **2021**, *60*, 13278.
[5] A. Dewaele, P. Loubeyre, M. Mezouar, *Phys. Rev. B.* **2004**, *70*, 094112.
[6] S. Anzellini, A. Dewaele, F. Occelli, P. Loubeyre, M. Mezouar, *J. Appl. Phys.* **2014**, *115*, 043511.
[7] M. M. Armentrout, A. Kavner, *J. Appl. Phys.* **2010**, *107*, 093528.
[8] L. Dubrovinsky, N. Dubrovinskaia, E. Bykova, M. Bykov, V. Prakapenka, C. Prescher, K. Glazyrin, H. P. Liermann, M. Hanfland, M. Ekholm, Q. Feng, L. V. Pourovskii, M. I. Katsnelson, J. M. Wills, I. A. Abrikosov, *Nature* **2015**, *525*, 226.
[9] a) C. Pantea, I. Mihut, H. Ledbetter, J. B. Betts, Y. Zhao, L. L. Daemen, H. Cynn, A. Migliori, *Acta. Mater.* **2009**, *57*, 544; b) M. B. Weinberger, S. H. Tolbert, A. Kavner, *Phys. Rev. Lett.* **2008**, *100*, 045506; c) G. A. Voronin, C. Pantea, T. W. Zerda, L. Wang, Y. Zhao, *J. Phys. Chem. Solids* **2005**, *66*, 706; d) F. Occelli, D. L. Farber, J. Badro, C. M. Aracne, D. M. Teter, M. Hanfland, B. Canny, B. Couzinet, *Phys. Rev. Lett.* **2004**, *93*, 095502; e) T. Kenichi, *Phys. Rev. B* **2004**, *70*, 012101.
[10] W. M. S. Hulm, J. K. Pessall, N., *Phys* **1971**, *55*, 60.
[11] R. A. Hein, *Phys. Rev.* **1956**, *102*, 1511.
[12] J. C. Phillips, *J. Appl. Phys.* **1972**, *43*, 3560.
[13] A. N. Christensen, W. Kress, M. Miura, N. Lehner, *Phys. Rev. B* **1983**, *28*, 977.
[14] a) X. Zhou, C. Gu, G. Song, D. Ma, L. Fang, C. Zhou, Y. Zhao, Y. Liang, S. Wang, *Chem. Mater.* **2022**, *34*, 9261; b) N. P. Salke, K. Xia, S. Fu, Y. Zhang, E. Greenberg, V. B. Prakapenka, J. Liu, J. Sun, J.-F. Lin, *Phys. Rev. Lett.* **2021**, *126*, 065702; c) W. Xing, Z. Wei, R. Yu, F. Meng, *J. Mater. Sci. Technol.* **2019**, *35*, 2297; d) T. Sasaki, T. Ikoma, K. Sago, Z. Liu, K. Niwa, T. Ohsuna, M. Hasegawa, *Inorg. Chem.* **2019**, *58*, 16379; e) F. Kawamura, H. Yusa, T. Taniguchi, *J. Am. Ceram. Soc.* **2018**, *101*, 949; f) H. Yusa, F. Kawamura, T. Taniguchi, N. Hirao, Y. Ohishi, T. Kikegawa, *J. Appl. Phys.* **2014**, *115*, 103520; g) D. Li, F. Tian, D. Duan, K. Bao, B. Chu, X. Sha, B. Liu, T. Cui, *RSC Adv.* **2014**, *4*, 10133; h) S. Wang, X. Yu, Z. Lin, R. Zhang, D. He, J. Qin, J. Zhu, J. Han, L. Wang, H.-k. Mao, J. Zhang, Y. Zhao, *Chem. Mater.* **2012**, *24*, 3023; i) R. Hrubiak, V. Drozd, A. Karbasi, S. K. Saxena, *J. Appl. Phys.* **2012**, *111*, 112612; j) T. Chihi, J. C. Parlebas, M. Guemmaz, *Phys. Status Solidi B* **2011**, *248*, 2787; k) A. Friedrich, B. Winkler, L. Bayarjargal, W. Morgenroth, E. A. Juarez-Arellano, V. Milman, K. Refson, M. Kunz, K. Chen, *Phys. Rev. Lett.* **2010**, *105*, 085504; l) A. Zerr, G. Miehe, J. Li, D. A. Dzivenko, V. K. Bulatov, H. Höfer, N. Bolfan-Casanova, M. Fialin, G. Brey, T. Watanabe, M. Yoshimura, *Adv. Funct. Mater.* **2009**, *19*, 2282; m) C. Jiang, Z. Lin, Y. Zhao, *Phys. Rev. Lett.* **2009**, *103*, 185501; n) J.-C. Zheng, *Phys. Rev. B* **2005**, *72*, 052105; o) V. V. S. Xiao-Jia Chen, Z. Wu, M. Somayazulu, J. Qian, S. Kung, A. N. Christensen, Y. Zhao, R. E. Cohen, M. Ho-kwang, R. J. Hemley, *Proc. Natl. Acad. Sci. USA* **2005**, *102*, 3198; p) E. Gregoryanz, C. Sanloup, M. Somayazulu, J. Badro, G. Fiquet, H. K. Mao, R. J. Hemley, *Nat. Mater.* **2004**, *3*, 294; q) A. Zerr, G. Miehe, R. Riedel, *Nat. Mater.* **2003**, *2*, 185; r) J. S. Shah, M. E. Straumanis, *J. Appl. Phys.* **2003**, *42*, 3288; s) C.-S. Y. Hyunchae Cynn, *Phys. Rev. B* **1999**, *59*, 8526; t) M. H. Mueller, *Scr. Metall.* **1977**, *11*, 693; u) L.-G. Liu, T. Takahashi, W. A. Bassett, *J. Phys. Chem. Solids* **1970**, *31*, 1345; v) H. P. Singh, *Acta Cryst.* **1968**, *A24*, 469; w) G. V. Samsonov, in *Handbook of the Physicochemical Properties of the Elements*, (Ed: G. V. Samsonov), Springer US, Boston, MA **1968**, p. 387. x) P. A. Romans, O. G. Paasche, H. Kato, *J. Less-Common. Met.* **1965**, *8*, 213; y) B. N. Dutta, B. Dayal, *Phys. Status Solidi B* **1963**, *3*, 473; z) E. A. Owen, E. W. Roberts, *Z. fur Krist. – Cryst. Mater.* **1937**, *96*, 497; aa) W. P. Davey, *Phys. Rev.* **1925**, *25*, 753.
[15] A. Dewaele, F. Datchi, P. Loubeyre, M. Mezouar, *Phys. Rev. B* **2008**, *77*, 094106.
[16] a) ALMONTY, https://almonty.com/tungsten/demand-pricing/, (accessed: November 2023); b) STRATEGIC METALS INVEST, https://strategicmetalsinvest.com/rhenium-prices/(accessed: November 2023); c) V. Kankhva, K. Argimbaev, D. Ligotsky, E. Loginov, *E3S Web of Conferences* **2021**, 258, e12012.
[17] C. Wang, Q. Tao, S. Dong, X. Wang, P. Zhu, *Inorg. Chem.* **2017**, *56*, 3970.
[18] M. Bykov, S. Chariton, E. Bykova, S. Khandarkhaeva, T. Fedotenko, A. V. Ponomareva, J. Tidholm, F. Tasnadi, I. A. Abrikosov, P. Sedmak, V. Prakapenka, M. Hanfland, H. P. Liermann, M. Mahmood, A. F. Goncharov, N. Dubrovinskaia, L. Dubrovinsky, *Angew. Chem., Int. Ed.* **2020**, *59*, 10321.
[19] M. Miao, Y. Sun, E. Zurek, H. Lin, *Nat. Rev. Chem.* **2020**, *4*, 508.
[20] R. S. Ningthoujam, N. S. Gajbhiye, *Prog. Mater. Sci.* **2015**, *70*, 50.
[21] J. W. Gibson, R. A. Hein, *Phys. Rev. Lett.* **1964**, *12*, 688.
[22] a) Y. Wang, E. Zhao, J. Zhao, L. Fu, C. Ying, L. Lin, *Comput. Mater. Sci.* **2019**, *156*, 215; b) M. J. Mehl, D. Finkenstadt, C. Dane, G. L. W. Hart, S. Curtarolo, *Phys. Rev. B* **2015**, *91*, 184110.
[23] Y. Fei, A. Ricolleau, M. Frank, K. Mibe, G. Shen, V. Prakapenka, *Proc. Natl. Acad. Sci. USA* **2007**, *104*, 9182.
[24] S. Asano, K. Niwa, T. Sasaki, N. A. Gaida, M. Hasegawa, *Inorg. Chem.* **2020**, *59*, 7915.
[25] D. Laniel, B. Winkler, T. Fedotenko, A. Aslandukova, A. Aslandukov, S. Vogel, T. Meier, M. Bykov, S. Chariton, K. Glazyrin, V. Milman, V. Prakapenka, W. Schnick, L. Dubrovinsky, N. Dubrovinskaia, *Phys. Rev. Mater.* **2022**, *6*, 023402.
[26] T. Sasaki, T. Yamamoto, S. Asano, K. Niwa, M. Hasegawa, *Dalton Trans.* **2023**, *52*, 469.
[27] R. Yu, Q. Zhan, L. C. De Jonghe, *Angew. Chem., Int. Ed.* **2007**, *46*, 1136.
[28] P. C. Müller, C. Ertural, J. Hempelmann, R. Dronskowski, *J. Phys. Chem. C* **2021**, *125*, 7959.
[29] A. D. Becke, K. E. Edgecombe, *J. Chem. Phys.* **1990**, *92*, 5397.
[30] A. Savin, R. Nesper, S. Wengert, T. F. Fässler, *Angew. Chem., Int. Ed.* **1997**, *36*, 1808.
[31] M. Wessel, R. Dronskowski, *J. Am. Chem. Soc.* **2010**, *132*, 2421.
[32] V. E. Bondybey, J. W. Nibler, *J. Chem. Phys.* **1973**, *58*, 2125.
[33] P. B. Allen, R. C. Dynes, *Phys. Rev. B* **1975**, *12*, 905.
[34] E. G. Maksimov, S. Q. Wang, M. V. Magnitskaya, S. V. Ebert, *Supercond. Sci. Technol.* **2009**, *22*, 075004.
[35] a) E. Thorwarth, M. Dietrich, C. Politis, *Solid State Commun.* **1976**, *20*, 869; b) F. M. Kilbane, P. S. Habig, *J. Vac. Sci. Technol.* **1975**, *12*, 107.
[36] E. Bailey, P. F. McMillan, *J. Mater. Chem.* **2010**, *20*, 4176.
[37] V. L. Ginzburg, L. D. Landau, *Zh. Eksp. Teor. Fiz.* **1950**, *20*, 1064.
[38] a) F. Birch, *Phys. Rev.* **1947**, *71*, 809; b) F. D. Murnaghan, *Proc. Natl. Acad. Sci. USA* **1944**, *30*, 244.
[39] M. T. Yeung, R. Mohammadi, R. B. Kaner, *Annu. Rev. Mater. Res.* **2016**, *46*, 465.
[40] R. M. Hazen, L. W. Finger, *J. Geophys. Res.* **1979**, *84*, 6723.
[41] Z. T. Y. Liu, D. Gall, S. V. Khare, *Phys. Rev. B* **2014**, *90*, 134102.
[42] F. M. Gao, J. L. He, E. D. Wu, S. M. Liu, D. L. Yu, D. C. Li, S. Y. Zhang, Y. J. Tian, *Phys. Rev. Lett.* **2003**, *91*, 015502.
[43] J. J. Gilman, *J. Appl. Phys.* **1975**, *46*, 5110.

[44] J. Wright, C. Giacobbe, M. Majkut, *Curr. Opin. Solid State Mater. Sci.* **2020**, *24*, 100818.
[45] H. P. Liermann, Z. Konopkova, W. Morgenroth, K. Glazyrin, J. Bednarcik, E. E. McBride, S. Petitgirard, J. T. Delitz, M. Wendt, Y. Bican, A. Ehnes, I. Schwark, A. Rothkirch, M. Tischer, J. Heuer, H. Schulte-Schrepping, T. Kracht, H. Franz, *J. Synchrotron Radiat.* **2015**, *22*, 908.
[46] *CrysAlisPRO, Oxford Diffraction /Agilent Technologies UK Ltd*, Oxford, UK **2019**.
[47] A. Aslandukov, M. Aslandukov, N. Dubrovinskaia, L. Dubrovinsky, *J. Appl. Cryst.* **2022**, *55*, 1383.
[48] G. M. Sheldrick, *Acta. Cryst.* **2015**, *71*, 3.
[49] O. V. Dolomanov, L. J. Bourhis, R. J. Gildea, J. A. K. Howard, H. Puschmann, *J. Appl. Cryst.* **2009**, *42*, 339.
[50] C. Prescher, V. B. Prakapenka, *High Press. Res.* **2015**, *35*, 223.
[51] J. Rodríguez-Carvajal, *Phys. B* **1993**, *192*, 55.
[52] a) P. Giannozzi, O. Baseggio, P. Bonfa, D. Brunato, R. Car, I. Carnimeo, C. Cavazzoni, S. de Gironcoli, P. Delugas, F. Ferrari Ruffino, A. Ferretti, N. Marzari, I. Timrov, A. Urru, S. Baroni, *J. Chem. Phys.* **2020**, *152*, 154105; b) P. Giannozzi, O. Andreussi, T. Brumme, O. Bunau, M. Buongiorno Nardelli, M. Calandra, R. Car, C. Cavazzoni, D. Ceresoli, M. Cococcioni, N. Colonna, I. Carnimeo, A. Dal Corso, S. de Gironcoli, P. Delugas, R. A. DiStasio, A. Ferretti, A. Floris, G. Fratesi, G. Fugallo, R. Gebauer, U. Gerstmann, F. Giustino, T. Gorni, J. Jia, M. Kawamura, H. Y. Ko, A. Kokalj, E. Kucukbenli, M. Lazzeri, et al., *J. Phys., Condens. Matter* **2017**, *29*, 465901; c) P. Giannozzi, S. Baroni, N. Bonini, M. Calandra, R. Car, C. Cavazzoni, D. Ceresoli, G. L. Chiarotti, M. Cococcioni, I. Dabo, A. Dal Corso, S. de Gironcoli, S. Fabris, G. Fratesi, R. Gebauer, U. Gerstmann, C. Gougoussis, A. Kokalj, M. Lazzeri, L. Martin-Samos, N. Marzari, F. Mauri, R. Mazzarello, S. Paolini, A. Pasquarello, L. Paulatto, C. Sbraccia, S. Scandolo, G. Sclauzero, A. P. Seitsonen, et al., *J. Phys., Condens. Matter* **2009**, *21*, 395502.
[53] P. E. Blochl, *Phys. Rev. B* **1994**, *50*, 17953.
[54] J. P. Perdew, K. Burke, M. Ernzerhof, *Phys. Rev. Lett.* **1996**, *77*, 3865.
[55] S. Grimme, J. Antony, S. Ehrlich, H. Krieg, *J. Chem. Phys.* **2010**, *132*, 154104.
[56] H. J. Monkhorst, J. D. Pack, *Phys. Rev. B* **1976**, *13*, 5188.
[57] K. Xia, H. Gao, C. Liu, J. Yuan, J. Sun, H. T. Wang, D. Xing, *Sci. Bull.* **2018**, *63*, 817.
[58] S. Maintz, V. L. Deringer, A. L. Tchougreeff, R. Dronskowski, *J. Comput. Chem.* **2016**, *37*, 1030.
[59] X.-Q. Chen, H. Niu, D. Li, Y. Li, *Intermetallics* **2011**, *19*, 1275.
[60] A. Togo, I. Tanaka, *Scr. Mater.* **2015**, *108*, 1.
[61] S. Baroni, S. de Gironcoli, A. Dal Corso, P. Giannozzi, *Rev. Mod. Phys.* **2001**, *73*, 515.